CELL-INTEGRATED SENSING FUNCTIONALITIES FOR SMART BATTERY SYSTEMS WITH IMPROVED PERFORMANCE AND SAFETY

GA 957273

D2.1 – REPORT ON SELECTION OF INKS AND PASTES

LC-BAT-13-2020 - Sensing functionalities for smart battery cell chemistries

Deliverable No.	2.1	
Related WP	2	
Deliverable Title	Report on selection of inks and pastes with different rheological properties and solvent formulations	
Deliverable Date	28-02-2021	
Deliverable Type	REPORT	
Dissemination level	Public (PU)	
Written By	Sebastiano Bellani (BDM) Francesco Bonaccorso (BDM)	18-02-2021 18-02-2021
Checked by	Francesco Bonaccorso (BDM) Sebastiano Bellani (BDM)	26-02-2021 26-02-2021
Reviewed by	Prasanna Kadirvelayutham (ABEE) Silvia Bodoardo (POL) Iñigo Gandiaga (IIE)	23-02-2021 25-02-2021 26-02-2021
Approved by	Iñigo Gandiaga (IKE)	26-02-2021
Status	Final	26-02-2021

Summary

The following deliverable D.2.1 "report on selection of inks and pastes" summarizes the activities and the corresponding results related to the Task 2.1 of the WP2, whose main objective is the realization of novel sensing technology based on printed electrodes enabling in situ Electrochemical Impedance Spectroscopy (EIS) and reliable in operando measurement of the electrolyte conductivity and its change during the cell operation. More specifically, Task 2.1 aimed to the development of inks and pastes for inkjet printing and screen printing of novel sensor electrodes, respectively. Subtask 2.1.1 focused on the selection and production methods for the electrode-materials.

Different materials, including single-/few-layer graphene (SLG/FLG), reduced graphene oxide (RGO), carbon black (CB), lithium titanate (LTO) and lithium iron phosphate (LFP) have been tested for inks and pastes formulation and printability. The SLG/FLG flakes were preferred to both as-produced and commercial RGO because of their superior chemical and structural quality, corresponding to electrically conductive paste with low electrical resistivity (on the order of 0.01 Ωcm). The SLG/FLG were produced by means of wet-jet milling exfoliation of bulk graphite, providing an effective route to scale-up the ink/paste technology (current SLG/FLG production rate = 1 kg/week) without recurring to chemical methods. The inks/pastes containing the selected materials have been formulated in Subtask 2.1.2. In particular, the selected electrode-materials have been dispersed in several liquid vehicles containing binders, solvents (aqueous or organic), without requiring additional rheology modifiers to prevent aggregation and/or precipitation. The influence of the active materials volume fraction, as well as their shape and spatial arrangement have been carefully investigated through electrical (four-probe), mechanical (tensile test), microscopic (transmission electron microscopy -TEM- and atomic force microscopy -AFM-), thermogravimetric analysis (TGA) and spectroscopic (Raman spectroscopy) characterizations.

Based on the outcome of these tests, inks and pastes with different solvent formulations have been successfully formulated and allow us to select them for the execution of the Task 2.2. Preliminary flat-flex wires assembly and sample wiring, electrical resistance testing of the printed sensing electrodes, and pouch cell assembly have been investigated to evaluate the compatibility of the polymeric binders used in the sensing electrodes with the battery electrolyte. These activities will be continued during the next month in Task 2.2, in which all the typologies of sensing electrodes developed by BDM will be in-depth characterized through in situ and in operando techniques.

This deliverable and the related task does not include any deviation from the objectives and timings planned in the Grant Agreement of the SENSIBAT project.

Table of Contents

1 Introduction 7

2 Development of inks and pastes 8

2.1.1 Selection of materials 8

2.1.2 Formulation of printable inks and pastes 12

3 Cells assembly and preliminary tests 15

3.1 Pastes and sampling 15

3.2 Flat-flex wires assembly and sample wiring 15

3.3 Tests 17

3.3.1 Electrical resistance testing 17

3.3.2 Electrolyte compatibility tests 17

3.4 Pouch-like assembly 18

3.4.1 Electrodes evaluation after 24 hours 19

4 Discussion & Conclusion 20

5 Risks 21

6 References 22

7 Acknowledgement 25

List of Figures and Tables

Figure 1. Scheme of the WJM system, the arrows indicate the flow of the solvent.

Figure 2. a) TEM image of WJM-produced SLG/FLG and b) statistical analysis of their lateral size. c) AFM image of WJM-produced SLG/FLG and d) statistical analysis of their thickness. e) Comparison between the Raman spectra of the starting graphite and WJM-produced SLG/FLG flakes. Their multi-peak Lorentzian fitting shows the contributions of the different 2D modes (orange line: $2D_1$; blue line: $2D_2$). f) Raman statistical analysis of the $I(2D_1)/I(G)$ *vs.* $I(2D_2)/I(G)$ plot for the SLG/FLG.

Figure 3. Examples of carbon electrically conductive films deposited on: a) glass substrate (microscope slides); b) plastics (Polyethylene terephthalate -PET-); c) paperboard.

Figure 4. AFM images of four different samples films deposited on glass substrates.

Figure 5. Example of sensing electrodes printed on Celgard 2500 through screen printing (left panel) and stencil printing (right panel).

Figure 6. a) Render of the whole assembly; b) exploded assembly with explosion guidelines: (a) Upper Celgard 2500, (b) upper Kapton stiffener, (c) upper Kapton strips, (d) copper connector, (e) bottom Kapton strips, (f) printed Celgard 2500, (g) bottom Kapton stiffener. Graphene-based printed electrodes are shown in black colour.

Figure 7. Scheme of the whole assembly reporting dimensions of the printed electrodes. Dimensions are all in mm. Bottom side of the device is reproduced.

Figure 8. Pictures of the assembled devices before electrolyte compatibility tests and coffee-bag embedding. (a) Sample 3 - 1, (b) Sample 3 - 2, (c) Sample 4 - 1, (d) Sample 4 - 2.

Figure 9. Conductive tracks of a Sample 4-1 electrodes swelling.

Figure 10. Four complete bags with embedded electrodes. Sample 3-1–1, Sample 3 1-2, Sample 3-2-1, Sample 3-2-2.

Table 1. Electrical performances of the films obtained by depositing representative pastes properly optimized with different polymer (see Section 2.1.1) on rigid glass substrates.

Table 2. Composition of three different pastes developed in task 2.1.

Table 3. Samples name and quantity supplied by BDM to POL.

Table 4. Resistance values measured for BDM electrodes and assembly electrodes/wires.

Abbreviations

Symbol / Abbreviation	
AC	*Alternate current*
ACR	*Acrylates*
AFM	*Atomic force microscopy*
CB	*Carbon Black*
DC	*Direct current*
DEC	*Diethyl carbonate*
DMF	*N,N-Dimethylformamide*
EC	*Ethylene carbonate*
EIS	*Electrochemical impedance spectroscopy*
EMC	*Ethyl methyl carbonate*
GO	*Graphene oxide*
LFP	*Lithium iron phosphate ($LiFePO_4$)*
LTO	*Lithium titanate ($Li_4Ti_5O_{12}$)*
NMP	*N-Methyl-2-pyrrolidone*
PC	*Polycarbonate*
PET	*Polyethylene terephthalate*
PPSU	*Polyphenylsulfone*
PU	*Polyurethane*
PVB	*Polyvinyl butyral*
PVDF	*Polyvinylidene difluoride*
RGO	*Reduced graphene oxide*
RMS	*Root mean squared*
SLG/FLG	*Single-/few-layer graphene*
TEM	*Transmission electron microscopy*
TGA	*Thermogravimetric Analysis*
WJM	*Wet-jet milling*
WP	*Work Package*

1 Introduction

One of SENSIBAT's overall objective is to develop a sensing technology for Li-ion batteries that measures in real-time cell's impedance (separately for the anode, cathode, and electrolyte) and the internal battery electrolyte conductivity. In the WP2, novel sensing technology consisting of printed reference electrodes that enables *in situ* Electrochemical Impedance Spectroscopy (EIS) and reliable *in operando* measurement of the electrolyte conductivity and its change during the cell operation will be developed.

The D2.1 report, summarizes the activities related to the Task 2.1 of WP2 carried out by BDM (WP Leader) with the support of POL. More in detail, this task (split in Subtask 2.1.1 and Subtask 2.1.2) concerned the development of inks and pastes for printing of electrodes for electrochemical sensing in Li-ion batteries.

- Subtask 2.1.1 focused on the selection and production methods for the electrode-materials.
- The inks/pastes containing the selected materials were developed in Subtask 2.1.2.

The obtained results, in term of rheological and electrical/mechanical/thermal properties of the formulated inks/pastes achieved the performances required by the SENSIBAT project. In fact, the films produced through printing techniques show resistivity as low as 0.01 Ω·cm and withstand tensile strains significantly superior to 50%. The obtained data allow us to use and test the developed materials in Task 2.2, thus continuing the WP activities. In this context, preliminary flat-flex wires assembly and sample wiring, electrical resistance testing of the printed sensing electrodes, and pouch cell assembly have been investigated to evaluate the compatibility of the polymeric binders used in the sensing electrodes with the battery electrolyte, i.e., $LiPF_6$ EC:DEC (1:1) 1 M commercial electrolyte. These activities will be continued in Task 2.2, by characterizing all the typologies of sensing electrodes developed by BDM.

2 Development of inks and pastes

This chapter describes in detail the technical developments of inks and pastes for printing of electrodes for electrochemical sensing in Li-ion batteries. First, we briefly explain the process followed for the material selection, then the formulation of printable inks and pastes with the selected materials are shown in detail. As mentioned before, the obtained properties of the formulated inks/pastes, will allow the development of printed electrodes on cell components (separator) in the Task 2.2 of the SENSIBAT project.

2.1.1 Selection of materials

The following electrically conductive materials have been screened for the formulation of sensing electrodes:

- SLG/FLG: Single-/few-layer graphene
- RGO: Reduced graphene oxide
- CB: Carbon Black

The SLG/FLG have been produced through wet-jet milling (WJM) exfoliation of graphite in N-Methyl-2-pyrrolidone (NMP, see **Figure 1**).[1,2]

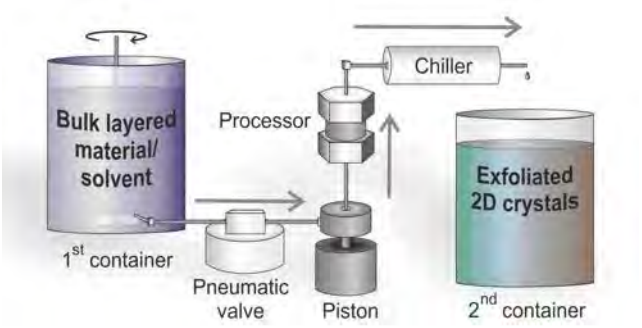

Figure 1. Scheme of the WJM system, the arrows indicate the flow of the solvent.

In brief, a mixture including 20 L of NMP (> 97%, Sigma Aldrich) and 200 g of graphite flakes (+100 mesh, Sigma Aldrich) was prepared in a container and mixed by a mechanical stirrer (Eurostar digital Ika-Werke). Subsequently, the mixture was pressurized by a hydraulic piston into a processor consisting of five sets of different perforated and interconnected disks by applying a pressure in the range of 140 to 250 MPa. Two jet streams originated at the second disk, which is made of two holes with a diameter of 1 mm in diameter. Then, the jet streams collided in the channel between the second and the third disks, *i.e.*, a nozzle with diameter of 0.3 mm. During the passage of the sample through the nozzle, the turbulence of the solvent originated the shear force causing the exfoliation of the graphite. The theoretical details of the exfoliation mechanism have been discussed in ref. 1. The as-produced dispersion was cooled down by a chiller and then collected in another container. To obtain the final SLG/FLG dispersion, the sample was re-processed by WJM apparatus three times, passing consecutively through nozzles with diameters of 0.2, 0.15 and 0.1 mm, respectively. The as-produced SLG/FLG dispersion was dried in form of powder by means of a rotary evaporator and the primary solvent (*i.e.*, NMP) was then exchanged with a secondary one, *i.e.*, dimethyl sulfoxide (DMSO). The mixture was poured into Petri dishes and subsequently transferred into a freeze dryer machine, to obtain the final freeze-dried SLG/FLG powder.

We used two different sources of RGO. The first one was purchased from Graphenea, while the second one was produced by BDM. Standard commercial syntheses of RGO are based on the (modified) Hummers method,[3,4,5] in which graphite is previously oxidized by a solution of potassium permanganate in sulfuric acid to produce

graphene oxide (GO) via a subsequent exothermic reaction. Afterwards, GO can be reduced using hydrazine to partially recover its sp^2-bonded carbon network.[6,7] However, hydrazine is highly toxic and can even functionalize GO with nitrogen heteroatoms,[8] altering the properties of pristine graphene.[9,10] Alternatives to hydrazine, $NaBH_4$, ascorbic acid, and HI, just to cite a few, can be used for the reduction of GO.[11]

The GO synthesized by BDM started from the oxidation of graphite flakes using a modified Hummer's method. Briefly, 1 g of graphite and 0.5 g of sodium nitrate (Sigma Aldrich) were mixed, followed by the addition of 25 mL of sulphuric acid. After 4 h, 3 g of potassium permanganate was added slowly to the above mixture, keeping the temperature at 4 °C with the aid of an ice bath. The mixture was let to react at room temperature overnight and the resulting dispersion was diluted by adding 2 L of distilled water under stirring. Finally, the sample was filtered and rinsed with water.

Instead of resorting chemical methods typically used for the production of commercial RGO, we reduced our GO by thermal annealing in a quartz tube passing through a three-zones split furnace. Under a 100 sccm flow of Ar/H_2 (90/10), 100 mg of GO were heated to 100 °C for 20 min to remove the presence of water residuals. Subsequently, a ramp of 20 °C/min was used to reach 1000 °C, and stabilized at this temperature for 2 h. Finally, the oven is left to cool down until reaching room temperature.

The manufacture of RGO has been widely developed at industrial level with massive production rates.[12] However, the residual oxygen, heteroatoms and structural defects in the RGO structure deteriorate the electrical, mechanical and tribological properties of pristine graphene.[13,14] Despite the advantage of pristine graphene, its massive production has been less established so far. In this context, the WJM approach developed by BDM allowed massive production rate of pristine graphene in form of SLG/FLG (~0.4 g min^{-1} on a single WJM apparatus).[1,2] Based on the WJM technology, BDM developed a pilot line for the production of SLG/FLG powder with a production capability of 1 kg/week.

Based on the above consideration, as well as preliminary tests on electrically conductive pastes, SLG/FLG were preferred to RGO (both the as-produced and commercial ones) as two-dimensional carbonaceous electrically conductive materials. The choice was motivated by their excellent chemical purity (percentage atomic content -at%- of sp^2 C > 95%, as detected by X-ray photoelectron spectroscopy), high electrical conductivity (*e.g.*, carbon pastes with conductivity approaching to 100 S cm^{-1}, as measured by four-probe method) and superior mechanical properties compared to RGO (as measured in our previous works through microscopic tribological tests *via* AFM equipment).[14,15,16] For the sake of clarity, XPS analysis of RGO revealed a residue of sp^3 C at% of 8.5%, as well as an at% of carbon in O–C=O bonds of 3.8%. The corresponding carbon pastes showed a conductivity inferior to 10 S cm^{-1}, almost one order of magnitude lower than the reference products based on WJM-produced SLG/FLG.

Carbon black is also a commercially available product, widely used as electrically conductive additives in electrodes for energy storage systems and electrically conductive carbon paste. For this project, CB powder was purchased from Alfa Aesar (Super P® Conductive). The CB nanoparticles act as effective spacers between graphene flakes, avoiding the re-stacking of the latter,[16] while electrically connecting the graphene flakes.[16,17] These effects have been used for the development of low-resistivity carbon pastes.[15]

Figure 2 reports the morphological and structural characterization of WJM-produced SLG/FLG. The TEM image of representative WJM-produced SLG/FLG sample (**Figure 2a**) evidences flakes with regular borders. The TEM statistical analysis of the lateral size of the SLG/FLG (**Figure 2b**) shows a lognormal distribution peaked at ~619 nm. **Figure 2c** reports an AFM image of a nanometre (nm) thick SLG/FLG flake. The AFM statistical analysis of

the thickness of the SLG/FLG (**Figure 2d**) indicates that the data follow a lognormal distribution peaked at ~2.20 nm, confirming that the sample mainly consists of SLG/FLG. Raman spectroscopy measurements were carried out to further confirm the structural quality of the WJM-produced SLG/FLG. The typical Raman spectrum of exfoliated graphene flakes shows, as fingerprints, the G (E_{2g} phonon at the Brillouin zone centre, ~1585 cm^{-1})[18–20] D (breathing modes of sp^2 rings requiring a defect for its activation by double resonance, ~1380 cm^{-1})[18,20–22], D' (~1620 cm^{-1})[23] and 2D (~2700 cm^{-1}) [20] peaks. We refer to the specific literature for the exhaustive explanation of the Raman peaks.[18–25] Importantly, the 2D peak is an excitation wavelength-dependent single peak (centered at ~2680 cm^{-1} at excitation wavelength of 514 nm) for SLG,[19,20,24] whereas is a superposition of $2D_1$ and $2D_2$ components, for FLG and graphite.[19,20,24] In graphite, the intensity of the $2D_2$ band is twice the $2D_1$ band,[19,20,26] **Figure 2e** shows the Raman spectra of the starting graphite and the WJM-produced SLG/FLG (normalized to the G peak intensity). The Raman spectrum of the WJM-produced SLG/FLG exhibits an increase of the D peak compared to those of pristine graphite, which is consistent with previous literature on exfoliated graphene flakes.[27–31] The analysis of the 2D peaks allows the flakes thickness to be estimated. In fact, the intensity of the $2D_2$ in graphite is around twice that of $2D_1$.[20,26]

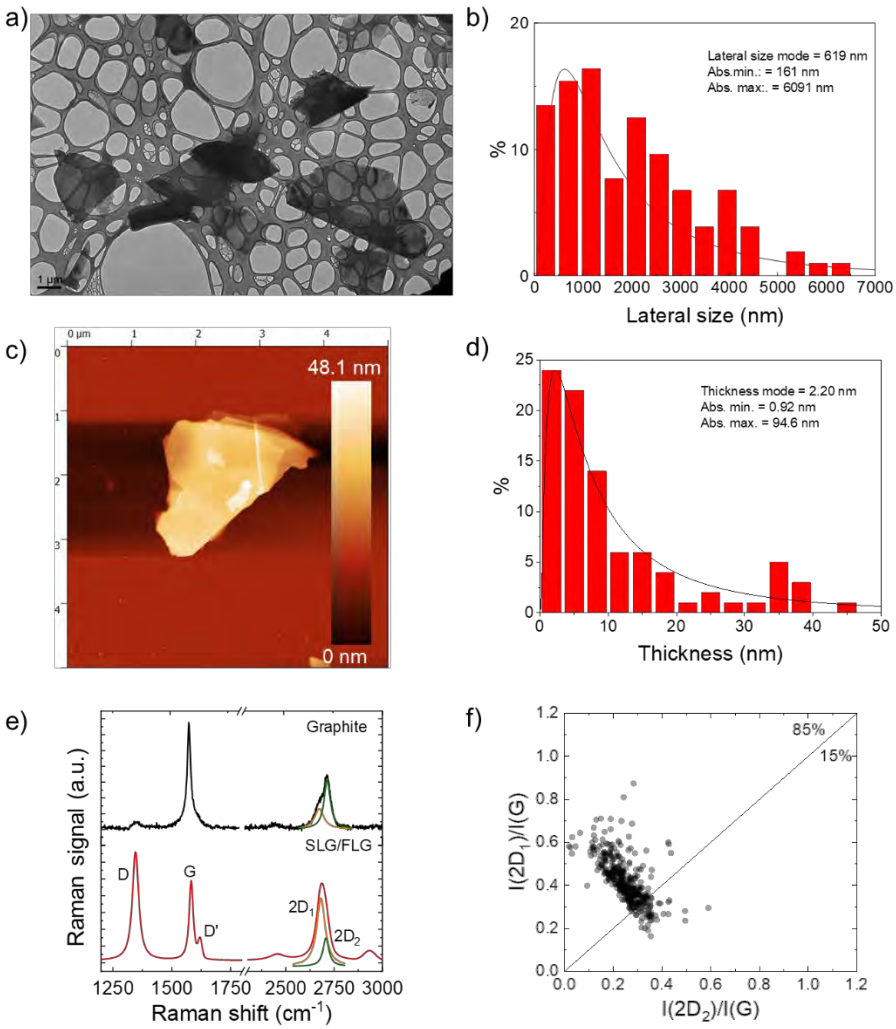

Figure 2. a) TEM image of WJM-produced SLG/FLG and b) statistical analysis of their lateral size. c) AFM image of WJM-produced SLG/FLG and d) statistical analysis of their thickness. e) Comparison between the Raman spectra of the starting graphite and WJM-produced SLG/FLG flakes. Their multi-peak Lorentzian fitting shows the contributions of the different 2D modes (orange line: $2D_1$; blue line: $2D_2$). f) Raman statistical analysis of the $I(2D_1)/I(G)$ *vs.* $I(2D_2)/I(G)$ plot for the SLG/FLG.

Multi-layer graphene (> 5 layers) exhibits a 2D peak that is almost identical, in terms of intensity and line shape, to the one of graphite.[27,32] Few-layer graphene, instead, has a $2D_1$ peak more intense than the $2D_2$.[20,26] Consequently, in the $I(2D_1)/I(G)$ *vs.* $I(2D_2)/I(G)$ plot the data that fall above that line ($I(2D_1) > I(2D_2)$) correspond to flakes with less than 5 layers, while those below ($I(2D_1) < I(2D_2)$) refer to flakes with more than 5 layers (indistinguishable from graphite[19,20]). **Figure 2f** reports the $I(2D_1)/I(G)$ *vs.* $I(2D_2)/I(G)$ plot for WJM-produced SLG/FLG, confirming that the exfoliated sample mainly consists of SLG and FLG (~85%)8,[33] which is consistent with the AFM results.

The following active materials have been selected for the formulation of printable reference electrodes:

- Anode: Lithium titanate ($Li_4Ti_5O_{12}$, LTO), (already advised in the project proposal) [34]
- Cathode: Lithium iron phosphate ($LiFePO_4$, LFP) [35]

We have chosen these material systems because they undergo two-phase reactions upon intercalation or deintercalation with Li, resulting in stable and constant equilibrium potential.[36] The latter are pivotal requirements for active materials intended for the formulation of reproducible and reliable reference electrodes.[37,38,39] In addition, both LTO and LFP have reaction potentials (1.5-1.6 and 3.4-3.5 V *vs.* Li/Li^+, respectively)[36] located inside the stability window of the ethylene carbonate (EC):ethyl methyl carbonate (EMC) electrolytes,[34] which have been selected within the SENSIBAT project framework. According to previous literature, an electrochemical preconditioning of these materials could be considered to oxidize them up to half of their total charge.[36] Noteworthy, the anode and cathode materials used for the Li-ion battery of the project (*i.e.*, graphite and lithium nickel manganese cobalt oxide (NMC), respectively) are not suitable active materials for the formulation of reference electrodes. In fact, contrary to LTO and LFP, their intercalation/de-intercalation potentials are not constant during the charge/discharge processes, and therefore it would be impossible an accurate and reliable control of their equilibrium potential. In particular, a slight change of their chemical state will imply a significant change of their equilibrium potential, impeding their operation as reference electrode materials.

Noteworthy, an ideal reference electrode must be non-polarizable, which means that the corresponding resistance must be minimized. Therefore, the hybridization of active materials with the electrically conductive materials selected by the project (SLG/FLG and CB) has been subject matter of Subtask 2.1.2. Since common potentiostats/galvanostats have input current lower than 100 pA, resistance of reference electrode up to 10 kΩ are, in principle, acceptable to avoid excessive voltage losses in D-mode. In AC-mode (*e.g.*, EIS test), the capacitance reference electrode is in series with its the electrode resistance. Therefore, the reference electrode acts as a low-pass RC filter, whose RC constant must be maximized to guarantee a wide band operation umntil frequency of tens/hundreds of kHz, such as those used in EIS experiments to check the electrolyte conductivity. Therefore, non-porous morphologies are recommended for the reference electrode. This means that both electrically conductive and active nanomaterials must be incorporated in polymeric matrixes to form compact films.

Therefore, the following polymers with different mechanical and chemical characteristics have been screened for both the formation of reference materials and printable electrically conductive pastes:

- Polyvinylidene difluoride (PVDF)
- Poly(vinyl butyral) (PVB)
- Polyurethane (PU)
- Polycarbonate (PC)

- Acrylates (ACR)
- Polyphenylsulfone (PPSU)

Depending on the polymer to dissolve, different solvents such as DMF, NMP, ethanol, isopropanol were screened and used for the final formulation.

2.1.2 Formulation of printable inks and pastes

Hundreds of metal-free electrically conductive inks/pastes have been evaluated by systematically varying the SLG/FLG:CB weight ratio (from 100:0 to 0:100), while changing the percentage weight (wt%) of the electrically conductive materials relatively to the total solid content (including the polymeric component) (from 10 to 75 wt%). Preliminary tests on printing inks for ink-jet printing have revealed the need to carry out a high number of printing passes to deposit a conductive film. Moreover, the typical dimension of the ink-jet nozzle implies intrinsic limitation on both the morphology of the solid components and the overall ink rheology. In particular, the lateral size of the two-dimensional fillers must be reduced to avoid the clogging of the nozzle. However, this printing requirement negatively affect the electrical conductivity of the overall inks. On the contrary, the pastes formulated for screen printing represent an easy-to-handle solution for the project needs. Thus, following these indications, we optimized the rheology of the pastes for their deposition *via* screen printing. An added value of the formulated pastes relies on the fact that they can also be processed for stencil printing, using doctor blading method.

The pastes were optimized by balancing electrical, mechanical, and thermal performances, while checking their processability *via* the aforementioned printing techniques.

All the products were deposited by doctor blading or screen printing on both rigid and flexible substrates (*i.e.*, glass, plastics, and papers) (**Figure 3**).

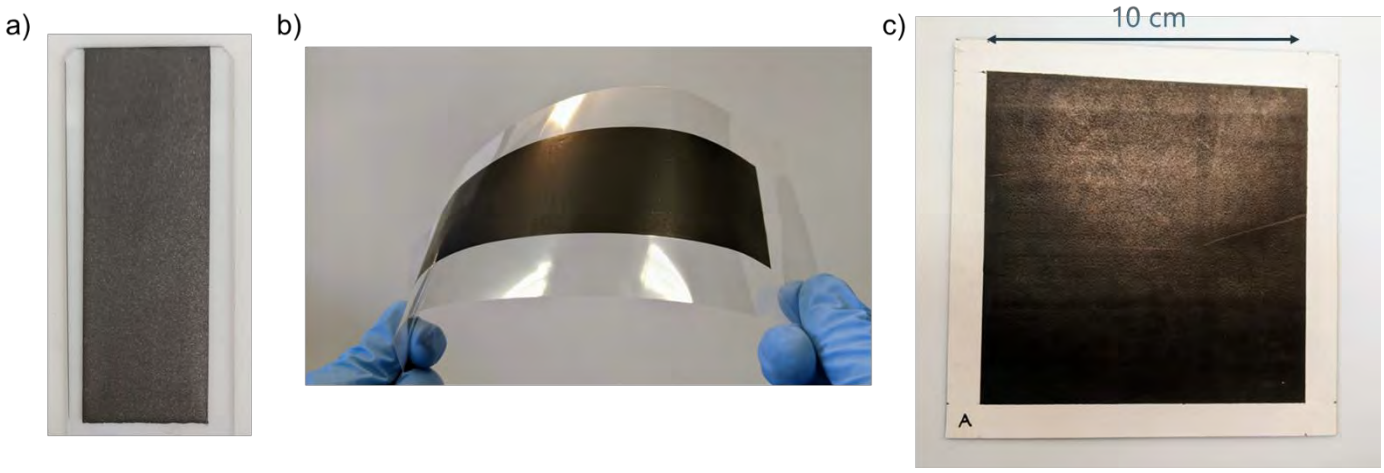

Figure 3. Examples of carbon electrically conductive films deposited on: a) glass substrate (microscope slides); b) plastics (Polyethylene terephthalate -PET-); c) paperboard.

The sheet resistances of the dried films were measured using a four-probe station (Jandel RM3000 Test Unit). The thicknesses of the films were then measured through a contact profilometer (XP-200, Ambios) to calculate the volumetric electrical resistivity and conductivity of each products, as summarized in **Table 1**.

Table 1. Electrical performances of the films obtained by depositing representative pastes properly optimized with different polymer (see Section 2.1.1) on rigid glass substrates.

Product name	Main components			Resistivity (Ω·cm)
	SLG/FLG	*CB*	*Polymer*	
Sample 1	*x*	*x*	*PVB*	*0.09 ± 0.01*
Sample 2	*x*		*PU:PC*	*0.03 ± 0.01*
Sample 3	*x*		*PPSU*	*0.02 ± 0.01*
Sample 4	*x*		*ACR*	*0.04 ± 0.01*
Sample 5	*x*	*x*	*PVDF*	*0.01 ± 0.01*

The mechanical properties of the films deposited on PET substrates were evaluated by measuring the electrical resistance as a function of the tensile strain. All the films withstand tensile strain significantly superior to 50%, until the fracture point of the PET substrate is reached (between 70-90%). Noteworthy, the elasticity and the mechanical strength of the sample is dictated by the substrates. However, sample 2 and sample 4 clearly exhibit the best resistance retention with increasing the tensile strength because of the superior flexibility and elasticity of their polymers compared to PPSU and PVB, which are however expected to show higher mechanical strength compared to PU:PC and ACR. In addition, thermogravimetric analysis (TGA) of the dried films demonstrate that they can withstand the operating temperature of Li-ion batteries (*i.e.*, -20 °C-60 °C).

The morphologies of the films printed by doctor blading on glass substrates were investigated through AFM measurements. **Figure 4** shows the AFM images of the investigated films, which exhibit root mean squared (RMS) roughness between 290 and 370 nm.

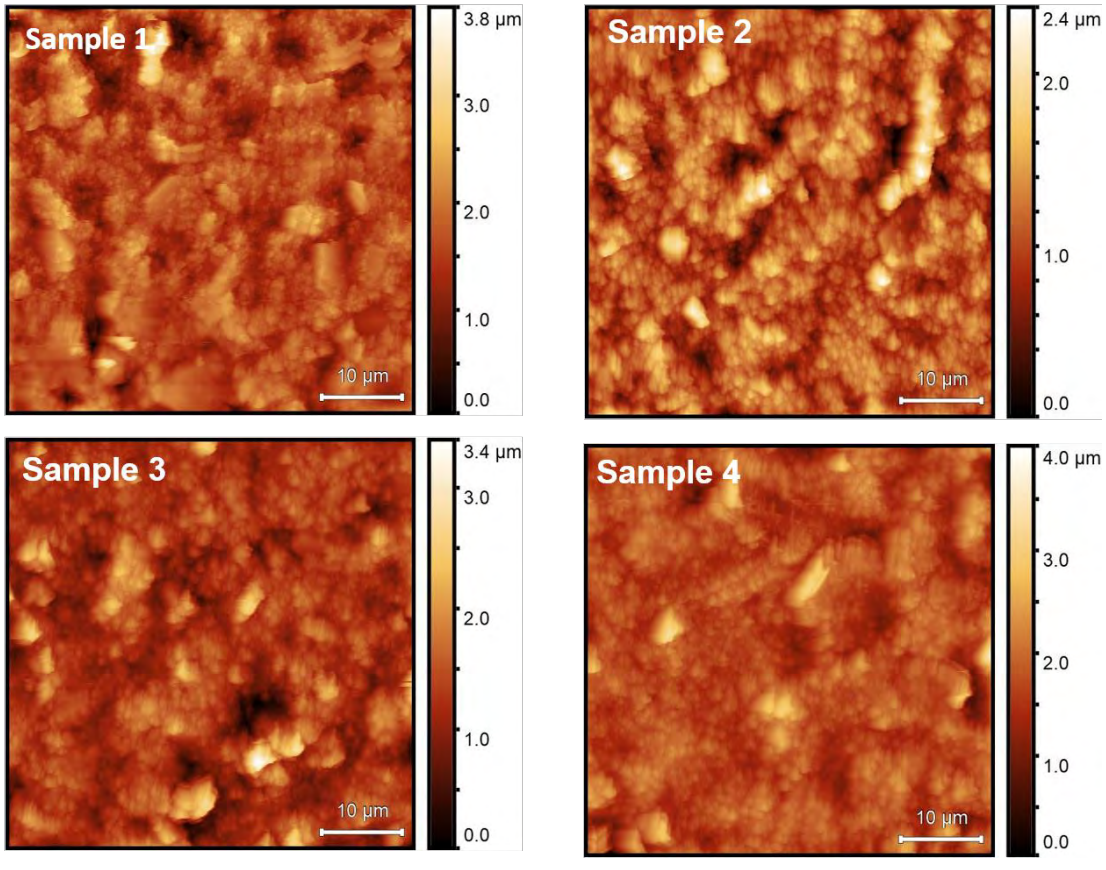

Figure 4. AFM images of four different samples films deposited on glass substrates.

The reference electrode pastes were formulated by modifying protocols reported in previous literature.[36] In order to understand the optimal material loading, as well as the mechanical properties and the printability, the following electrode material pastes were formulated.

Table 2. Composition of three different pastes developed in Task 2.1.

Product name	Component content (wt%)				Solvent
	Active material (LTO or LFP)	*PVDF*	*SLG/FLG*	*CB*	
Reference-A	25	25	25	25	NMP
Reference-B	50	25	12.5	12.5	NMP
Reference C	16.67	50	16.67	16.67	NMP

The first sensing electrode prototypes have been produced through screen printing and stencil printing on Celgard 2500 (**Figure 5**). The samples will be characterized by BDM and POL from M7 (Task 2.2) to assess their performance as electrodes for EIS tests and three-electrode configuration measurements in Li-ion batteries.

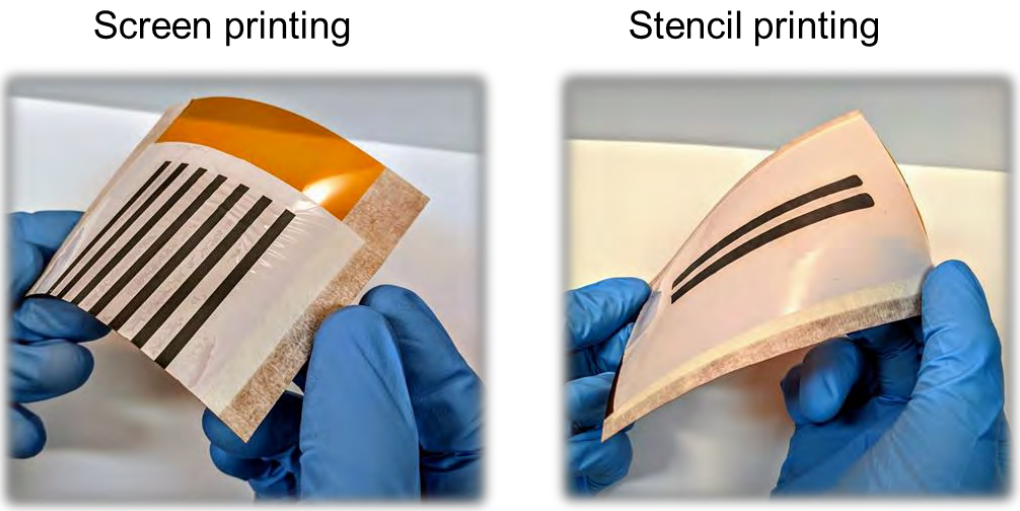

Figure 5. Example of sensing electrodes printed on Celgard 2500 through screen printing (left panel) and stencil printing (right panel).

3 Cells assembly and preliminary tests

POL started preliminary activities using the pastes formulated by BDM to develop printed sensing electrodes (electrically conductive electrodes and reference electrodes). These electrodes were characterized through *in situ* and *in operando* Electrochemical Impedance Spectroscopy (EIS) inside small pouch cells. As shown in **Figure 5**, the sensing electrodes have been printed directly on commercial separators (Celgard 2500).

3.1 Pastes and sampling

Four BDM pastes were first printed using a stencil printing technique on Celgard 2500 to form a pair of electrically conductive electrodes. The BDM samples used by POL are listed in **Table 3**.

Table 3. Samples name and quantity supplied by BDM to POL.

Sample	Solvent	Binder	Quantity	Tracks width (mm)	Tracks distance (mm)
Sample 3 - 1	*NMP*	***PPSU***	1	3	4
Sample 3 -2	*NMP*	***PPSU***	1	3	4
Sample 4 - 1	*water*	***ACR***	1	5	4
Sample 4 - 2	*water*	***ACR***	1	5	4

The samples were classified according to the solvent used in the manufacturing process/kind of polymer (1 or 2) used as binder. In particular, Sample 3 -1 and Sample 3-2 refer to electrode based on PPSU binder, while sample 4 – 1 and Sample 4 -2 refer to electrode based on ACR binder. Other type of samples will be investigated during the activities of the next task (Task 2.2, M6-M22).

The as-received electrodes consisted of a series of printed conductive tracks with a length of 8-10 cm, from which a set of shorter and smaller samples were cut to be positioned in coffee bags.

For each sample, at least two sub-samples were obtained by manually cutting the printed separator. Standard dimensions of cut sub-samples were chosen with the aim of manufacturing sub-samples with acceptable reproducibility in geometry (size and area).

3.2 Flat-flex wires assembly and sample wiring

In order to achieve a proper sealing of the coffee bags, it is mandatory to develop flat, thin and flex wires that interferes as less as possible during cell packaging bonding. Briefly, the process consists in the thermal bonding of the coffee bag edges under external uniaxial pressure, as achieved using a commercial bag-sealer. A rigid or excessively thick wire could cause partial sealing, inducing electrolyte leaching and/or moisture infiltration inside the cell, thus compromising its stability over time and functionality. Moreover, wires must be properly separated, without directly contacting the electrodes, except for the terminals.

To avoid the aforementioned issues, a simple approach was chosen for the preliminary stage of the work, which will be continued during the activity of the Task 2.2.

5x50 mm^2 (or 5x 60mm^2) pure copper strips (thickness 25 µm) were manually cut from a commercial copper sheet. Then, a set of 2 identical stripes of 20 µm-thick polyimide tape (1 Mil Kapton HN tape) of 5x40 mm^2 (or 5x50mm^2) were crafted and bonded on the upper and lower surface of the copper strip. This should ensure electrical insulation from the electrodes and chemical insulation from the electrolyte contained in the coffee bag. The thickness of the whole assembly is around 155 µm (65 µm for each Kapton tape and 25 µm for the

copper layer), a value that seems reasonable for a proper embedding in a standard pouch cell bag during the sealing process.

The flat-flex wires were then carefully aligned on the graphene composite tracks printed on Celgard 2500 sub-samples and manually bonded using a layer of the same Kapton tape. The Kapton layer is 10x25 mm^2. A second identical layer of Kapton tape was bonded on the opposite face of the Celgard separator, to act like a stiffener and ensure the electrolyte does not permeate directly in the copper-graphene junction and Kapton-Celgard interface. This could cause possible tape detachment due to adhesive silicon layer corruption/sliding, so must be avoided. Finally, a piece of Celgard 2500 with the same dimensions of the printed one was attached on the upper side of the whole assembly to simulate the real configuration in the cell. Upper Celgard patch will be used like electrolyte-permeable electrical insulator to avoid short circuit of the tracks due to contact within the upper cell electrodes. Everything was handcrafted, so small differences between the assemblies might be possible.

A scheme of the whole assembly setup is shown in **Figure 6a,b**. **Figure 7** shows the real quotes for the assembly. It should be noticed that, in the current configuration, the electrolyte permeates into the Celgard and will inevitably contact the copper connectors. Therefore, alternative strategies or suitable equivalent circuit modelling will be developed for the correct interpretation of the electrode sensing behaviour.

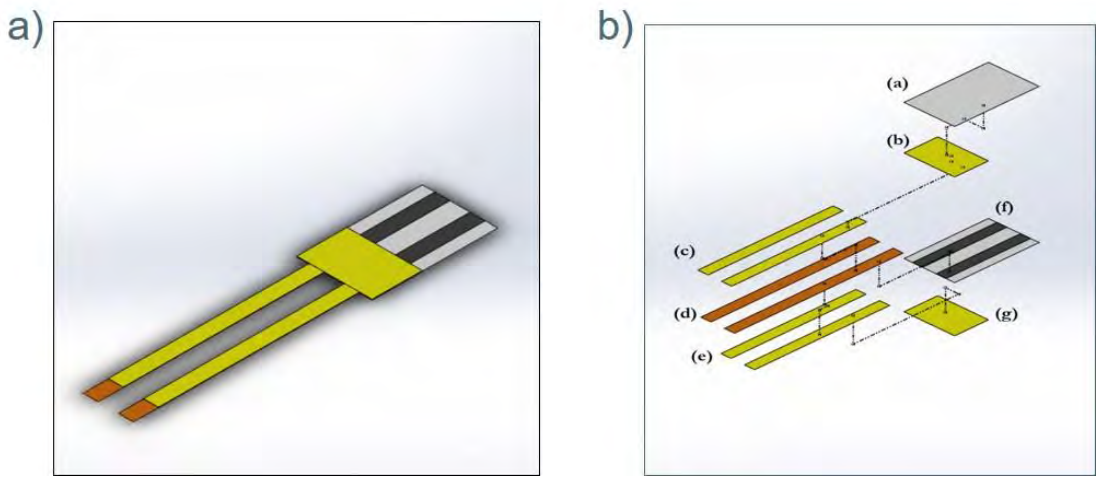

Figure 6. a) Render of the whole assembly; b) exploded assembly with explosion guidelines: (a) Upper Celgard 2500, (b) upper Kapton stiffener, (c) upper Kapton strips, (d) copper connector, (e) bottom Kapton strips, (f) printed Celgard 2500, (g) bottom Kapton stiffener. Graphene-based printed electrodes are shown in black colour.

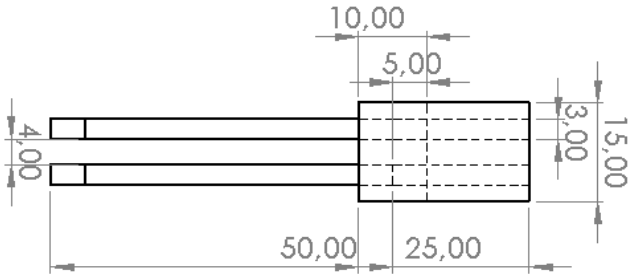

Figure 7. Scheme of the whole assembly reporting dimensions of the printed electrodes. All dimensions are in mm. Bottom side of the device is reproduced.

The process of wiring and assembly was repeated two times for every sample. Finally, eight sub-samples (2 for each composition) fully wired and properly insulated were collected for the next step. Pictures of the eight assemblies are reported below in **Figure 8**:

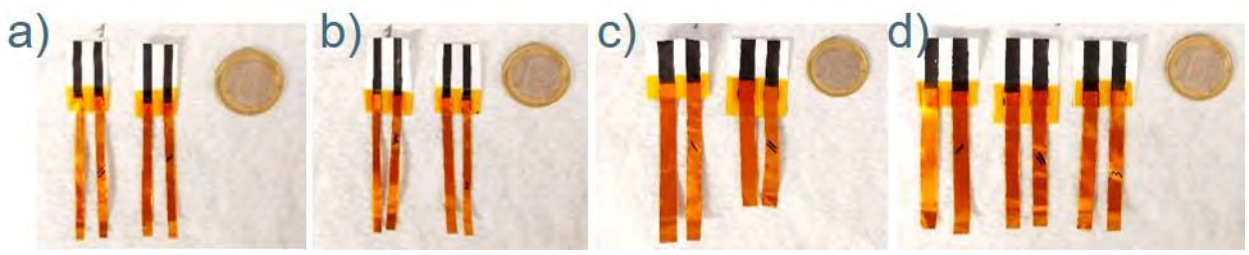

Figure 8. Pictures of the assembled devices before electrolyte compatibility tests and coffee-bag embedding. (a) Sample 3 - 1, (b) Sample 3 - 2, (c) Sample 4 - 1, (d) Sample 4 - 2.

3.3 Tests

3.3.1 Electrical resistance testing

The electrical resistance of each graphene strip was checked before and after wiring using a laboratory multimeter (Keithley DMM 6500) using a simple two-wires probe method. Resistance was evaluated at the extremes of each sub-sample track. Resistance of copper flat-flex wires was also checked in the same way, resulting a value <0.002 Ωcm^{-1}. Resistance of the assembled graphene electrodes plus copper flat-flex wires was finally considered. Considering that wire resistance is negligible compared to the one of the graphene electrodes, the whole resistance is equal to the resistance for cm from the upper side of the graphene electrodes to the wire front on Celgard. Obviously, this second value should be lower than the point to point 25 mm resistance of the graphene electrode (for sake of clarity, it would be ideally a value according to the 2nd Ohm law, but except the contribution of the contact resistance between copper-graphene surfaces that is unknown). The results are summarized in the **Table 4**.

Table 4. Resistance values measured for BDM electrodes and assembly electrodes/wires.

Sample	Track 1 R point to point (25 mm) (Ωcm^{-1})	Track 2 R point to point (25 mm) (Ωcm^{-1})	Track 1 Graphene-wire resistance (20 mm) (Ωcm^{-1})	Track 2 Graphene-wire resistance (20 mm) (Ωcm^{-1})
Sample 3-1-1	292	295	275	285
Sample 3 -1-2	248	236	245	235
Sample 3-2-1	148	148	145	150
Sample 3-2-2	196	156	180	145
Sample 4-1-1	72	64	51	50
Sample 4-1-2	76	80	51	51
Sample 4-2-1	48	41	39	57
Sample 4-2-2	49	44	54	59

3.3.2 Electrolyte compatibility tests

To unravel the compatibility of the proposed assembly towards the real cell environment, each sample was dipped for 30 minutes in a $LiPF_6$ EC:DEC (1:1) 1 M commercial electrolyte (Solvionic).

Sample 3-1 and Sample 3-2 do not show any sign of degradation. Conversely, Sample 4-1 and Sample 4-2 evinced a significant degradation already after a few minutes of rinsing in the electrolyte. Evident swelling of conductive tracks, detachment from the Celgard substrate and finally solubilization inside the electrolyte were observed. Probably, this is due a chemical incompatibility between the polymeric binder used in the printing process and the composition of the electrolyte. So, this set of samples were discarded. **Figure 9** reports the condition of one of water-based electrodes after rinsing.

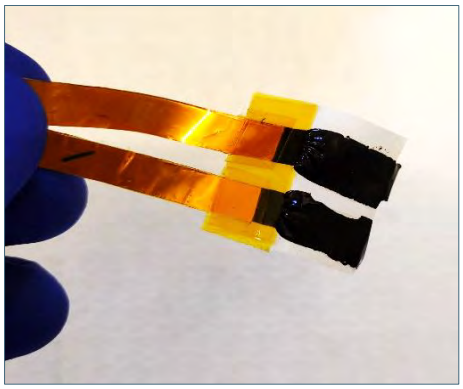

Figure 9. Conductive tracks of a Sample 4-1 electrodes swelling.

3.4 Pouch-like assembly

The assembly of the pouch-like configuration was done without anode, cathode and contact tabs. The aim of the assembly was to preliminary evaluate the proper sealing of the system for the subsequent activities of Task 2.2.

Bags of 50x50 mm^2 were assembled and sealed, at the edges and borders, through a thermal-pressure method. The coffee bags were made of aluminium/thermoplastic polymer composite that bonds itself during heating under uniaxial pressure. This was done on two of the three sealable sides. On the flat-flex wiring side, additional layers of thermoplastic stiffener tape and thermo-bonding adhesive layers were used to ensure a proper sealing. Before embedding, every sample was rinsed in the electrolyte to ensure an adequate pre-wetting. The same process was carried out with the additional Celgard patch.

25 drops (approximatively 1.5 ml) of electrolyte were dripped inside the bag before final sealing. The electrolyte quantity was exaggerated to be sure that the sensor remains completely wet. The whole assembly process was done in a dry environment (dry-room). **Figure 10** shows the completed bags within embedded printed Celgard.

Figure 10. Four complete bags with embedded electrodes. Sample 3-1–1, Sample 3 1-2, Sample 3-2-1, Sample 3-2-2.

3.4.1 Electrodes evaluation after 24 hours

The integrity of the printed sensing electrodes was evaluated after 24 hours from the realization. One bag was opened and the printed Celgard condition assessed. As shown in Figure 11, no evident electrodes modification was observable. The bag was still full of electrolyte, so there is no evidence of electrolyte leakage. This is linked with the proper sealing process. Therefore, the as-designed assembly configuration has been selected for the electrochemical tests planned for the Task 2.2 of the project.

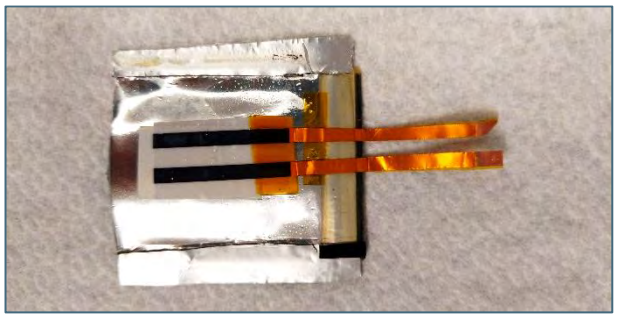

Figure 11. Opened bag with intact electrodes

4 Discussion & Conclusion

We have investigated different electrically conductive and/or electrochemically active materials, including single-/few-layer graphene (SLG/FLG), reduced graphene oxide (RGO), carbon black (CB), lithium titanate (LTO) and lithium iron phosphate (LFP) for the formulation of inks and pastes for the printing of novel sensing electrodes for Li-ion batteries. Meanwhile, various polymeric materials, including polyvinylidene difluoride (PVDF), poly (vinyl butyral) (PVB), polyurethane (PU), polycarbonate (PC), acrylates (ACR), polyphenylsulfone (PPSU) were screened as binding components into the ink/paste composition to print mechanically robust and flexible films.

Among the two-dimensional electrically conductive materials, the SLG/FLG flakes were preferred to other graphene-based materials (*e.g.*, RGO) because of their superior chemical and structural quality, corresponding to electrically conductive paste with low electrical resistivity (on the order of 0.01 Ω·cm). The availability for the reproducibility of the results and the scalability of the process was also demonstrated in this task. In fact, the SLG/FLG were produced by means of wet-jet milling exfoliation, providing an effective route to scale-up the ink/paste technology without recurring to chemical methods, while all the other materials (*i.e.*, CB, LTO, LFP) are commercially available. The CB nanoparticles were used as spherical electrically conductive nanomaterials since act as effective spacers between graphene flakes, avoiding the re-stacking of the latter, while providing effective electrical connections. The combination of SLG/FLG and CB resulted in high-conductivity (approaching to 100 S cm^{-1}) carbon pastes. Lastly, LTO and LFP were selected as electrode reference materials because they undergo two-phase reactions upon intercalation or deintercalation with Li, resulting in stable and constant equilibrium potential.

The rheology and mechanical/electrical/thermal properties of the inks/pastes have been optimized by systematically varying the SLG/FLG:CB weight ratio (from 100:0 to 0:100), while changing the percentage weight (wt%) of the electrically conductive materials relatively to the total solid content (including the polymeric component) (from 10 to 75 wt%). The pastes were optimized by optimally balancing electrical, mechanical, and thermal performances.

Deposition activities and their processability *via* printing techniques were also carried out. Preliminary tests on both inks for ink-jet printing and pastes for screen printing have shown superior electrical properties of the latter once deposited onto the substrate. For this reason, we optimized the rheology of the pastes to deposit them *via* screen printing. In addition, the pastes formulated for screen printing can also be processed through stencil printing. These two deposition systems are industrially relevant and ensure the scalability and industrial exploitation of the obtained results.

Based on the outcome of these tests, the optimized inks and pastes with different solvent formulations (see Tables 1,2) have been selected for the following Task 2.2 (Development of printed electrodes on cell components (separator)).

Based on the results obtained in task 2.1, preliminary activity of task 2.2 was already initiated. In fact, optimized pastes were used to print electrodes, *i.e.*, working, counter and reference electrodes. The electrodes were printed directly onto commercial separators (Celgard). In this framework, POL realized highly conductive flat-flexible and thin (flat-flex) wiring of printed Celgard samples. Meanwhile, POL produced small pouch cells (area ~5 cm^2) assembly within wired printed separators to evaluate the sealing of the system for the subsequent activities of Task 2.2. Lastly, POL checked the chemical compatibility of the printed tracks with the selected battery electrolyte.

5 Risks

Risk No.	What is the risk	Probability of risk occurrence[1]	Effect of risk[2]	Solutions to overcome the risk
WP2.1	*The tabs connecting the sensing electrodes printed on separator to external circuit will be contacted by the electrolyte. The tabs contacted by the battery electrolyte will contribute to the electrochemical response of the sensing electrodes*	*1*	*1*	*1. Printing sensing electrodes on non-permeable substrate that can be integrated in the battery configuration.* *2. Modelling of the tab contribution to the response of the sensing electrodes.*

[1] Probability risk will occur: 1 = high, 2 = medium, 3 = Low

[2] Effect when risk occurs: 1 = high, 2 = medium, 3 = Low

6 References

(1) Del Rio Castillo, A. E.; Pellegrini, V.; Ansaldo, A.; Ricciardella, F.; Sun, H.; Marasco, L.; Buha, J.; Dang, Z.; Gagliani, L.; Lago, E.; Curreli, N.; Gentiluomo, S.; Palazon, F.; Prato, M.; Oropesa-Nuñez, R.; Toth, P. S.; Mantero, E.; Crugliano, M.; Gamucci, A.; Tomadin, A.; Polini, M.; Bonaccorso, F. High-Yield Production of 2D Crystals by Wet-Jet Milling. *Mater. Horizons* **2018**, *5* (5), 890–904. https://doi.org/10.1039/C8MH00487K.

(2) Del Rio-Castillo, A. E.; Ansaldo, A.; Pellegrini, V.; Bonaccorso, F. Exfoliation Materials by Wet-Jet Milling Techniques. WO2017/089987A1, 2017.

(3) Marcano, D. C.; Kosynkin, D. V.; Berlin, J. M.; Sinitskii, A.; Sun, Z.; Slesarev, A.; Alemany, L. B.; Lu, W.; Tour, J. M. Improved Synthesis of Graphene Oxide. *ACS Nano* **2010**. https://doi.org/10.1021/nn1006368.

(4) Backes, C.; Abdelkader, A. M.; Alonso, C.; Andrieux-Ledier, A.; Arenal, R.; Azpeitia, J.; Balakrishnan, N.; Banszerus, L.; Barjon, J.; Bartali, R.; Bellani, S.; Berger, C.; Berger, R.; Ortega, M. M. B.; Bernard, C.; Beton, P. H.; Beyer, A.; Bianco, A.; Bøggild, P.; Bonaccorso, F.; Barin, G. B.; Botas, C.; Bueno, R. A.; Carriazo, D.; Castellanos-Gomez, A.; Christian, M.; Ciesielski, A.; Ciuk, T.; Cole, M. T.; Coleman, J.; Coletti, C.; Crema, L.; Cun, H.; Dasler, D.; De Fazio, D.; Díez, N.; Drieschner, S.; Duesberg, G. S.; Fasel, R.; Feng, X.; Fina, A.; Forti, S.; Galiotis, C.; Garberoglio, G.; García, J. M.; Garrido, J. A.; Gibertini, M.; Gölzhäuser, A.; Gómez, J.; Greber, T.; Hauke, F.; Hemmi, A.; Hernandez-Rodriguez, I.; Hirsch, A.; Hodge, S. A.; Huttel, Y.; Jepsen, P. U.; Jimenez, I.; Kaiser, U.; Kaplas, T.; Kim, H.; Kis, A.; Papagelis, K.; Kostarelos, K.; Krajewska, A.; Lee, K.; Li, C.; Lipsanen, H.; Liscio, A.; Lohe, M. R.; Loiseau, A.; Lombardi, L.; Francisca López, M.; Martin, O.; Martín, C.; Martínez, L.; Martin-Gago, J. A.; Ignacio Martínez, J.; Marzari, N.; Mayoral, Á.; McManus, J.; Melucci, M.; Méndez, J.; Merino, C.; Merino, P.; Meyer, A. P.; Miniussi, E.; Miseikis, V.; Mishra, N.; Morandi, V.; Munuera, C.; Muñoz, R.; Nolan, H.; Ortolani, L.; Ott, A. K.; Palacio, I.; Palermo, V.; Parthenios, J.; Pasternak, I.; Patane, A.; Prato, M.; Prevost, H.; Prudkovskiy, V.; Pugno, N.; Rojo, T.; Rossi, A.; Ruffieux, P.; Samorì, P.; Schué, L.; Setijadi, E.; Seyller, T.; Speranza, G.; Stampfer, C.; Stenger, I.; Strupinski, W.; Svirko, Y.; Taioli, S.; Teo, K. B. K.; Testi, M.; Tomarchio, F.; Tortello, M.; Treossi, E.; Turchanin, A.; Vazquez, E.; Villaro, E.; Whelan, P. R.; Xia, Z.; Yakimova, R.; Yang, S.; Yazdi, G. R.; Yim, C.; Yoon, D.; Zhang, X.; Zhuang, X.; Colombo, L.; Ferrari, A. C.; Garcia-Hernandez, M. Production and Processing of Graphene and Related Materials. *2D Mater.* **2020**, *7* (2), 22001. https://doi.org/10.1088/2053-1583/ab1e0a.

(5) Bonaccorso, F.; Lombardo, A.; Hasan, T.; Sun, Z.; Colombo, L.; Ferrari, A. C. Production and Processing of Graphene and 2d Crystals. *Mater. Today* **2012**. https://doi.org/10.1016/S1369-7021(13)70014-2.

(6) Krishnamoorthy, K.; Veerapandian, M.; Yun, K.; Kim, S. J. The Chemical and Structural Analysis of Graphene Oxide with Different Degrees of Oxidation. *Carbon N. Y.* **2013**. https://doi.org/10.1016/j.carbon.2012.10.013.

(7) Pei, S.; Cheng, H. M. The Reduction of Graphene Oxide. *Carbon N. Y.* **2012**. https://doi.org/10.1016/j.carbon.2011.11.010.

(8) Dreyer, D. R.; Park, S.; Bielawski, C. W.; Ruoff, R. S. The Chemistry of Graphene Oxide. *Chemical Society Reviews*. 2010. https://doi.org/10.1039/b917103g.

(9) Chua, C. K.; Pumera, M. Chemical Reduction of Graphene Oxide: A Synthetic Chemistry Viewpoint. *Chemical Society Reviews*. 2014. https://doi.org/10.1039/c3cs60303b.

(10) Eigler, S.; Hirsch, A. Chemistry with Graphene and Graphene Oxide - Challenges for Synthetic Chemists. *Angewandte Chemie - International Edition*. 2014. https://doi.org/10.1002/anie.201402780.

(11) Alam, S. N.; Sharma, N.; Kumar, L. Synthesis of Graphene Oxide (GO) by Modified Hummers Method and Its Thermal Reduction to Obtain Reduced Graphene Oxide (RGO)*. *Graphene* **2017**. https://doi.org/10.4236/graphene.2017.61001.

(12) Lin, L.; Peng, H.; Liu, Z. Synthesis Challenges for Graphene Industry. *Nature Materials*. 2019. https://doi.org/10.1038/s41563-019-0341-4.

(13) Zhu, Y.; James, D. K.; Tour, J. M. New Routes to Graphene, Graphene Oxide and Their Related Applications. *Advanced Materials*. 2012. https://doi.org/10.1002/adma.201202321.

(14) Garakani, M. A.; Bellani, S.; Pellegrini, V.; Oropesa-Nuñez, R.; Del RioCastillo, A. E.; Abouali, S.; Najafi, L.; Martín-García, B.; Ansaldo, A.; Bondavalli, P.; Demirci, C.; Romano, V.; Mantero, E.; Marasco, L.; Prato, M.; Bracciale, G.; Bonaccorso, F. Scalable Spray-Coated Graphene-Based Electrodes for High-Power Electrochemical Double-Layer Capacitors Operating over a Wide Range of Temperature. *Energy Storage Mater.* **2021**, *34*, 1–11.

(15) Bellani, S.; Najafi, L.; Zani, P.; Martin-Garcia, B.; Oropesa-Nunez, R.; Bonaccorso, F. Electrically Conductive Adhesive, 2020.

(16) Bellani, S.; Martín-García, B.; Oropesa-Nuñez, R.; Romano, V.; Najafi, L.; Demirci, C.; Prato, M.; Del Rio Castillo, A. E.; Marasco, L.; Mantero, E.; D'Angelo, G.; Bonaccorso, F. "Ion Sliding" on Graphene: A Novel Concept to Boost Supercapacitor Performance. *Nanoscale Horizons* **2019**. https://doi.org/10.1039/c8nh00446c.

(17) Phillips, C.; Al-Ahmadi, A.; Potts, S.-J.; Claypole, T.; Deganello, D. The Effect of Graphite and Carbon Black Ratios on Conductive Ink Performance. *J. Mater. Sci.* **2017**, *52* (16), 9520–9530. https://doi.org/10.1007/s10853-017-1114-6.

(18) Yang, L.; Deslippe, J.; Park, C.-H.; Cohen, M. L.; Louie, S. G. Excitonic Effects on the Optical Response of Graphene and Bilayer Graphene. *Phys. Rev. Lett.* **2009**, *103* (18), 186802. https://doi.org/10.1103/PhysRevLett.103.186802.

(19) Ferrari, A. C.; Meyer, J. C.; Scardaci, V.; Casiraghi, C.; Lazzeri, M.; Mauri, F.; Piscanec, S.; Jiang, D.; Novoselov, K. S.; Roth, S.; Geim, A. K. Raman Spectrum of Graphene and Graphene Layers. *Phys. Rev. Lett.* **2006**, *97* (18), 187401. https://doi.org/10.1103/PhysRevLett.97.187401.

(20) Ferrari, A. C.; Basko, D. M. Raman Spectroscopy as a Versatile Tool for Studying the Properties of Graphene. *Nat. Nanotechnol.* **2013**, *8*, 235.

(21) Ferrari, A. C.; Robertson, J. Interpretation of Raman Spectra of Disordered and Amorphous Carbon. *Phys. Rev. B* **2000**, *61* (20), 14095–14107. https://doi.org/10.1103/PhysRevB.61.14095.

(22) Ferrari, A. C.; Robertson, J. Resonant Raman Spectroscopy of Disordered, Amorphous, and Diamondlike Carbon. *Phys. Rev. B* **2001**, *64* (7), 75414. https://doi.org/10.1103/PhysRevB.64.075414.

(23) Su, C. Y.; Xu, Y.; Zhang, W.; Zhao, J.; Tang, X.; Tsai, C. H.; Li, L. J. Electrical and Spectroscopic Characterizations of Ultra-Large Reduced Graphene Oxide Monolayers. *Chem. Mater.* **2009**. https://doi.org/10.1021/cm902182y.

(24) Najafi, L.; Bellani, S.; Martín-García, B.; Oropesa-Nuñez, R.; Del Rio Castillo, A. E.; Prato, M.; Moreels, I.; Bonaccorso, F. Solution-Processed Hybrid Graphene Flake/2H-MoS2 Quantum Dot Heterostructures for Efficient Electrochemical Hydrogen Evolution. *Chem. Mater.* **2017**, *29* (14), 5782–5786. https://doi.org/10.1021/acs.chemmater.7b01897.

(25) Bellani, S.; Najafi, L.; Martín-García, B.; Ansaldo, A.; Del Rio Castillo, A. E.; Prato, M.; Moreels, I.; Bonaccorso, F. Graphene-Based Hole-Selective Layers for High-Efficiency, Solution-Processed, Large-Area, Flexible, Hydrogen-Evolving Organic Photocathodes. *J. Phys. Chem. C* **2017**, *121* (40), 21887–21903. https://doi.org/10.1021/acs.jpcc.7b05904.

(26) Dresselhaus, M. S.; Dresselhaus, G.; Hofmann, M. Raman Spectroscopy as a Probe of Graphene and Carbon Nanotubes. *Philos. Trans. R. Soc. A Math. Phys. Eng. Sci.* **2008**, *366* (1863), 231 LP – 236.

(27) Lucchese, M. M.; Stavale, F.; Ferreira, E. H. M.; Vilani, C.; Moutinho, M. V. O.; Capaz, R. B.; Achete, C. A.; Jorio, A. Quantifying Ion-Induced Defects and Raman Relaxation Length in Graphene. *Carbon N. Y.* **2010**, *48* (5), 1592–1597. https://doi.org/https://doi.org/10.1016/j.carbon.2009.12.057.

(28) Eckmann, A.; Felten, A.; Mishchenko, A.; Britnell, L.; Krupke, R.; Novoselov, K. S.; Casiraghi, C. Probing the Nature of Defects in Graphene by Raman Spectroscopy. *Nano Lett.* **2012**, *12* (8), 3925–3930. https://doi.org/10.1021/nl300901a.

(29) Ferrari, A. C. Raman Spectroscopy of Graphene and Graphite: Disorder, Electron–Phonon Coupling, Doping and Nonadiabatic Effects. *Solid State Commun.* **2007**, *143* (1), 47–57. https://doi.org/https://doi.org/10.1016/j.ssc.2007.03.052.

(30) Lotya, M.; Hernandez, Y.; King, P. J.; Smith, R. J.; Nicolosi, V.; Karlsson, L. S.; Blighe, F. M.; De, S.; Wang, Z.; McGovern, I. T.; Duesberg, G. S.; Coleman, J. N. Liquid Phase Production of Graphene by Exfoliation of Graphite in Surfactant/Water Solutions. *J. Am. Chem. Soc.* **2009**, *131* (10), 3611–3620. https://doi.org/10.1021/ja807449u.

(31) Cançado, L. G.; Jorio, A.; Ferreira, E. H. M.; Stavale, F.; Achete, C. A.; Capaz, R. B.; Moutinho, M. V. O.; Lombardo, A.; Kulmala, T. S.; Ferrari, A. C. Quantifying Defects in Graphene via Raman Spectroscopy at Different Excitation Energies. *Nano Lett.* **2011**, *11* (8), 3190–3196. https://doi.org/10.1021/nl201432g.

(32) Das, A.; Chakraborty, B.; Sood, A. K. Raman Spectroscopy of Graphene on Different Substrates and Influence of Defects. In *Bulletin of Materials Science*; 2008. https://doi.org/10.1007/s12034-008-0090-5.

(33) Bonaccorso, F.; Tan, P.-H.; Ferrari, A. C. Multiwall Nanotubes, Multilayers, and Hybrid Nanostructures: New Frontiers for Technology and Raman Spectroscopy. *ACS Nano* **2013**, *7* (3), 1838–1844. https://doi.org/10.1021/nn400758r.

(34) Yang, Z.; Choi, D.; Kerisit, S.; Rosso, K. M.; Wang, D.; Zhang, J.; Graff, G.; Liu, J. Nanostructures and Lithium Electrochemical Reactivity of Lithium Titanites and Titanium Oxides: A Review. *Journal of Power Sources*. 2009. https://doi.org/10.1016/j.jpowsour.2009.02.038.

(35) Zhang, W. J. Structure and Performance of LiFePO4 Cathode Materials: A Review. *Journal of Power Sources*. 2011. https://doi.org/10.1016/j.jpowsour.2010.11.113.

(36) La Mantia, F.; Wessells, C. D.; Deshazer, H. D.; Cui, Y. Reliable Reference Electrodes for Lithium-Ion Batteries. *Electrochem. commun.* **2013**. https://doi.org/10.1016/j.elecom.2013.03.015.

(37) Raccichini, R.; Amores, M.; Hinds, G. Critical Review of the Use of Reference Electrodes in Li-Ion Batteries: A Diagnostic Perspective. *Batteries*. 2019. https://doi.org/10.3390/batteries5010012.

(38) Dollé, M.; Orsini, F.; Gozdz, A. S.; Tarascon, J.-M. Development of Reliable Three-Electrode Impedance Measurements in Plastic Li-Ion Batteries. *J. Electrochem. Soc.* **2001**. https://doi.org/10.1149/1.1381071.

(39) Bünzli, C.; Kaiser, H.; Novák, P. Important Aspects for Reliable Electrochemical Impedance Spectroscopy Measurements of Li-Ion Battery Electrodes. *J. Electrochem. Soc.* **2015**. https://doi.org/10.1149/2.1061501jes.

7 Acknowledgement

The author(s) would like to thank the partners in the project for their valuable comments on previous drafts and for performing the review.

Project partners

#	PARTICIPANT SHORT NAME	PARTNER ORGANISATION NAME	COUNTRY
1	IKE	IKERLAN S. COOP.	Spain
2	BDM	BEDIMENSIONAL SPA	Italy
3	POL	POLITECNICO DI TORINO	Italy
4	FHG	FRAUNHOFER GESELLSCHAFT ZUR FOERDERUNG DER ANGEWANDTEN FORSCHUNG E.V.	Germany
5	FM	FLANDERS MAKE VZW	Belgium
6	TUE	TECHNISCHE UNIVERSITEIT EINDHOVEN	The Netherlands
7	NXP NL	NXP SEMICONDUCTORS NETHERLANDS BV	The Netherlands
8	NXP FR	NXP SEMICONDUCTORS FRANCE SAS	France
9	ABEE	AVESTA BATTERY & ENERGY ENGINEERING	Belgium
10	VAR	VARTA MICRO INNOVATION GMBH	Germany
11	AIT	AIT AUSTRIAN INSTITUTE OF TECHNOLOGY GMBH	Austria
12	UNR	UNIRESEARCH BV	The Netherlands

DISCLAIMER/ ACKNOWLEDGMENT

This project has received funding from the European Union's Horizon 2020 research and innovation programme under grant agreement No 957273. The information and views set out in this publication does not necessarily reflect the official opinion of the European Commission. Neither the European Union institutions and bodies nor any person acting on their behalf, may be held responsible for the use which may be made of the information contained therein.